ELSEVIER

Journal of Fluids and Structures 25 (2009) 321–342

JOURNAL OF FLUIDS AND STRUCTURES

www.elsevier.com/locate/jfs

Hydrodynamic and hydroelastic analyses of a plate excited by the turbulent boundary layer

E. Ciappi[a], F. Magionesi[a], S. De Rosa[b,*], F. Franco[b]

[a]*INSEAN-Istituto Nazionale per Studi ed Esperienze di Architettura Navale, Via di Vallerano 139, 00128 Roma, Italy*
[b]*ælab-Acoustics and Vibration Laboratory, Dipartimento di Ingegneria Aerospaziale, Università degli Studi di Napoli "Federico II", Via Claudio 21, 80125 Napoli, Italy*

Received 4 October 2007; accepted 11 April 2008
Available online 11 October 2008

Abstract

Recent studies have demonstrated that the characterisation of wall-pressure fluctuations for surface ships is of great interest not only for military applications but also for civil marine vehicles. A ship model towed in a towing tank is used to perform pressure and structural measurements at high Reynolds numbers. This facility provides ideal flow conditions because background turbulence and noise are almost absent. Free surface effects are naturally included in the analysis, although in the particular section chosen for the present study do not have significant consequences on pressure spectra. Scaling laws for the power spectral density are identified providing the possibility to estimate pressure spectra for different flow conditions and in particular for full-scale applications. The range of validity of some theoretical models for the cross-spectral density representation is analysed by direct comparison with experimental data of wall-pressure fluctuations measured in streamwise and spanwise direction. In a second phase, an indirect validation is performed by comparing the measured vibrational response of an elastic plate inserted in the catamaran hull with that obtained numerically using, as a forcing function, the modelled pressure load. In general, marine structures are able to accept energy mainly from the sub-convective components of the pressure field because the typical bending wavenumber values are usually lower than the convective one; thus, a model that gives an accurate description of the phenomenon at low wavenumbers is needed. In this work, it is shown that the use of the Chase model for the description of the pressure field provides a satisfactory agreement between the numerical and the experimental response of the hull plate. These experimental data, although acquired at model scale, represent a significant test case also for the real ship problem.

Keywords: Wall-pressure fluctuations; High Reynolds number flow; High-speed vessels; Theoretical models; Vibrational response

1. Introduction

Vibrations of elastic structures excited by the turbulent boundary layer (TBL) are of interest for interior and exterior noise emission problems in aeronautical, automotive and marine applications. In particular, new requirements in terms of comfort on board high-speed ships for passenger transportation have addressed the attention of the scientific community to the identification and to the characterisation of noise sources including those of hydrodynamic nature. Recent studies performed in the framework of the European RTD project NORMA (Noise Reduction for Marine

*Corresponding author: Tel.: +39 081 7683581; fax: +39 081 624609.
E-mail address: sergio.derosa@unina.it (S. De Rosa).

0889-9746/$ - see front matter © 2008 Elsevier Ltd. All rights reserved.
doi:10.1016/j.jfluidstructs.2008.04.006

Nomenclature

a	streamwise plate length
Area_i	equivalent area in finite element approach
b	spanwise plate length
c	speed of sound in water
c_B	bending wave speed
D	flexural stiffness of the plate
d	sensor dimension
d_0	nondimensional length: $d_0 = d/\delta^*$
d^+	nondimensional length: $d^+ = du_\tau/\nu$
Fr	Froude number
g	acceleration of gravity
$\mathbf{H}$	structural transfer function diagonal matrix
H	shape factor: $H = \delta^*/\vartheta$
h	thickness of the plate
i	imaginary unit
j	index for the jth modal component
k	acoustic wavenumber
k_c	convective wavenumber
k_B	bending wavenumber
L_{pp}	length between perpendiculars
m, n	modal indices
m^e	experimental added mass function
m^n	numerical added mass function
$\mathbf{N}$	shape function vector in finite element approach
NG	number of grid of the finite element mesh
NM	number of mode shapes
Re_ϑ	Reynolds number, $\mathrm{Re}_\vartheta = U\vartheta/\nu$
Re_τ	Reynolds number, $\mathrm{Re}_\tau = \delta u_\tau/\nu$
R_{pp}	cross-correlation function
S_{aa}	plate acceleration response (auto-spectral density)
$\mathbf{S}_\mathrm{W}$	matrix of the cross-spectral densities of the plate displacement
$\mathbf{S}_\Phi$	matrix of the cross-spectral densities of the generalised load
$\mathbf{S}_\mathrm{FF}$	matrix of the cross-spectral densities of the equivalent load
u^+	wall unit, $u^+ = U/u_\tau$
u_τ	friction velocity
U	free-stream velocity
U_c	convection velocity
x	streamwise reference axis
y	spanwise reference axis
y^+	wall unit, $y^+ = yu_\tau/\nu$

Greek symbols

γ_1	streamwise decay factor
γ_3	spanwise decay factor
Γ	coherence function
δ	boundary layer thickness
δ^*	displacement thickness
Δx	extension of each finite element in streamwise direction
Δy	extension of each finite element in spanwise direction
η	spanwise spatial separation
η_p	plate modal damping coefficient
ϑ	momentum thickness
θ	phase function
ν	kinematic viscosity
ξ	streamwise spatial separation
ρ_s	plate material density
ρ	fluid density
τ	time delay
τ_w	wall shear stress
Φ_{pp}	auto-spectral density of the wall-pressure distribution due to the turbulent boundary layer
$\Phi_{pp'}$	cross-spectral density of the wall-pressure distribution due to the turbulent boundary layer
$\mathbf{\Phi}$	eigenvector matrix
ω	circular radian frequency
ω_j	natural circular frequency of the jth mode
ω_{mn}	dry natural circular frequencies of the plate
$\tilde{\omega}_{mn}$	wet natural circular frequencies of the plate

Matrix and complex operators

*	complex conjugate operator
T	transposition operator

Applications G3RD-2001-0393) demonstrated that, at least for new concept design fast ships, flow noise sources, e.g., the TBL, play an important role above 30 knots.

The typical way to characterise wall-pressure fluctuations (WPF) is via experimental tests performed in suitable facilities like wind or water tunnels. In fact, direct numerical simulations (DNS) or large eddy simulations (LES) are often not applicable in the case of complex geometries and realistic flow conditions (high Reynolds numbers) due to the limitation of computational resources. DNS of WPF were performed by Choi and Moin (1990), analysing the channel flow problem for $\mathrm{Re}_\vartheta = U\vartheta/\nu = 287$. Furthermore, Chang et al. (1999) analysed the influence of the different TBL velocity components on the wavenumber pressure spectra in a channel flow for a Reynolds number, based on the channel half width, equal to 3200. Recently, Lee et al. (2005a) proposed a new methodology to calculate numerically wall-pressure spectra. The method uses the predicted mean flow field obtained from RANS calculations and a spectral

correlation model, and integrates across the TBL. The method was validated both for an equilibrium flow at $Re_\vartheta = 3582$ and for a non-equilibrium flow resulting from flow over a backward-facing step. Using the same methodology, Lee et al. (2005b) characterised wall-pressure spectra for a surface ship model including the effects of hull curvature and of the free surface. The comparison of the scaled spectra, obtained while varying the axial location, and the distance from the free surface with spectra, obtained for an equilibrium flow, showed that, in several locations, the former deviate from the canonical case.

On the other hand, there are many experimental works related to WPF, most of them devoted to the identification of the appropriate scaling laws for the auto-spectral density (ASD) for zero pressure gradient flow. The pressure ASD frequency range is subdivided according to the boundary layer regions that give contributions to wall-pressure spectra where different scaling variables hold. In particular, Farabee and Casarella (1991) identified four frequency ranges in their data: the low-frequency and the mid-frequency range where outer variables hold, the high-frequency range where inner variables hold, and an overlap scale-independent region proportional to ω^{-1}, whose extent depends on the Reynolds number. With respect to this point, Keith et al. (1992) presented the most extensive comparison among many available experimental data obtained in fully developed and developing channel flow, in fully developed pipe flow and in wind tunnel, over a wide range of Reynolds numbers, with the aim of identifying the best choice for the scaling parameters in the different frequency regions. Goody (1999) performed an experimental campaign in a two-dimensional boundary layer for Re_ϑ values ranging from 7800 to 23 400, investigating different combinations of scaling parameters. Finally, a detailed review of the state-of-the-art on this subject can be found in Bull (1996).

The spatial characterisation of WPFs was first analysed by Corcos (1963) on the basis of measurements performed by Willmarth and Wooldridge (1962). Assuming the validity of separation of variables in the streamwise and spanwise directions, Corcos stated an exponential decay for the cross-spectral density (CSD) as a function of the similarity variables $\omega\xi/U_c$ and $\omega\eta/U_c$, where U_c is the convection velocity, and ξ and η are the streamwise and spanwise spatial separation, respectively. Several authors have performed comparisons between measured CSD data and Corcos model (Blake, 1986; Bull, 1967); in particular, Farabee and Casarella (1991) from the analysis of their experimental data provided, at least in a certain nondimensional frequency range, a confirmation of this pressure behaviour for a wide series of spatial separations in streamwise direction and for different flow velocities or local Reynolds number values. The success of the Corcos model lies in its simplicity and in its predictive character since the model parameters are substantially case-independent. Nevertheless, it is generally stated that Corcos model gives a correct representation of the WPF behaviour in the convective domain, i.e. when the wavenumbers are close to the convective wavenumber $k_c = \omega/U_c$. On the contrary, in the sub-convective domain the white Corcos spectrum largely overpredicts the real amplitude. Since for several applications and in particular in the case of underwater and surface marine vehicles, the convective wavenumber is greater than the bending wavenumber $k_B = \omega/c_B$, it is of primary importance to evaluate correctly the sub-convective domain of pressure spectra that corresponds to the high-sensitivity region for the structure.

Several new models, some directly derived by the Corcos one (Efimtsov, 1982; Ffowcs Williams, 1982), others overcoming the Corcos multiplicative approach such as those by Chase (1980) and Smol'yakov and Tkachenko (1991), were developed to improve the estimation of pressure spectra in this region. A comparison between the predictions of the radiated acoustic power by rectangular plates was carried out numerically by Graham (1997); it was performed for different test conditions and applying the above models. It was there concluded that the use of sophisticated models such as the Chase one is needed only for structures that do not exhibit coincidence, but that for aircraft the best model is the one which provides an accurate description of the convective peak, thus suggesting the use of the Efimtsov model. Nonetheless, no experimental evidence supporting these conclusions was reported in Graham's work. However, the spatial domain comparison between pressure experimental spectra and theoretical models cannot definitively indicate the best in describing the different wavenumber regions. It is usually possible to find a set of parameters for each model able to provide a good data fit. It is clear that most of the energy of WPF is concentrated around the convective peak and then any correlation data is mainly the representation of the convective character of the TBL. Unfortunately, only few experimental data concerning direct measurements of the wavenumber-frequency spectrum are available (Abraham, 1998; Choi and Moin, 1990; Panton and Robert, 1994; Farabee and Geib, 1991; Manoha, 1996) and, among them, a big spread of the spectra magnitude at low wavenumbers is present as reported for example by Hwang and Maidanik (1990).

In order to overcome the limitations of flow measurements, an indirect approach to estimate the validity of different models for WPF representation, based on the analysis of the response of simple elastic structures to the TBL load, is proposed here. The same idea was recently applied by Finnveden et al. (2005), who compared the measured response of a flat plate with those obtained numerically using modelled pressure loads. This work presented the first and, to the authors' best knowledge, the only correlation between aerodynamic and structural data measured in the same facility and with the same set-up. They suggested a modified version of the Corcos model by introducing a frequency and flow speed dependence on the parameters and of the Chase model by introducing two new parameters to better fit the

spanwise coherence to measurements. Despite the modifications made, the conclusion was that, above the aerodynamic coincidence ($k_c = k_B$), only the Chase model, that does not make use of the multiplicative approach, provides a fair agreement with experimental data. In this work, the lower k_B/k_c ratio was 0.4 and the average difference between the modified Chase model predictions and the experimental data was 5 dB. Furthermore, Hambric et al. (2004), although retaining the multiplicative approach, proposed a modification of Corcos streamwise coherence to better represent the low wavenumber domain. The model was compared with the experimental response of an elastic plate measured by Han et al. (1999). The ratio between the structural wavenumber in flow direction and the convective wavenumber was between 0.3 and 0.8 and the agreement with the experimental data was quite good. On the other hand, Han et al. (1999) chose Smol'yakov and Tkachenko to model the surface pressure field. The comparison with measurements was performed using the energy flow analysis method to predict the numerical plate response thus, direct information about the validity of the pressure model are difficult to extract from their data.

The aim of this work is to develop a general procedure based on the identification of the scaling laws and on the use of predictive models for the surface pressure field suitable for application to full-scale problems. In particular, the capabilities of Corcos and Chase models to predict the response of an elastic plate inserted in the hull of a ship model were investigated on the basis of hydrodynamic and vibration data acquired, at high Reynolds numbers, in a towing tank. In a first step, pressure data were analysed to provide their spectral characteristics. This analysis is fundamental to identify the scaling laws for the ASD and the free parameters contained in the CSD wall-pressure fluctuation models. The high Reynolds number achieved with this set-up provides an interesting extension to the previous analyses. In a second phase, a comparison between the numerical response of the plate obtained using the two models and the experimental response is provided. Since in the present problem the convection velocity is very low, the ratio between the bending and the convective wavenumber is sensibly lower than those previously analysed in the technical literature. This fact is fundamental for real size marine applications for which hydrodynamic coincidence appears, even for high-speed vehicles, at very low frequency.

This first section is aimed to frame the work in the proper existing literature. Section 2 presents the experimental set-up and all the data concerning the acquisition instrumentation. The treatment of the pressure data is the specific argument of Section 3. Section 4 is fully devoted to the analysis of the structural response and the final comparison between predictive and measured data. Section 5 presents the concluding remarks with some foreseen activities. For the sake of completeness, a graphic workflow has been also added in Chart 1.

2. Experimental set-up

2.1. Pressure measurements

The experiments were performed on a 1:15 scale model of the fast catamaran Jumbo CAT (Fig. 1). The scale of the model was chosen according to Froude similarity: $\mathrm{Fr} = U/\sqrt{gL_{pp}}$ where L_{pp} is the length between perpendiculars, i.e.

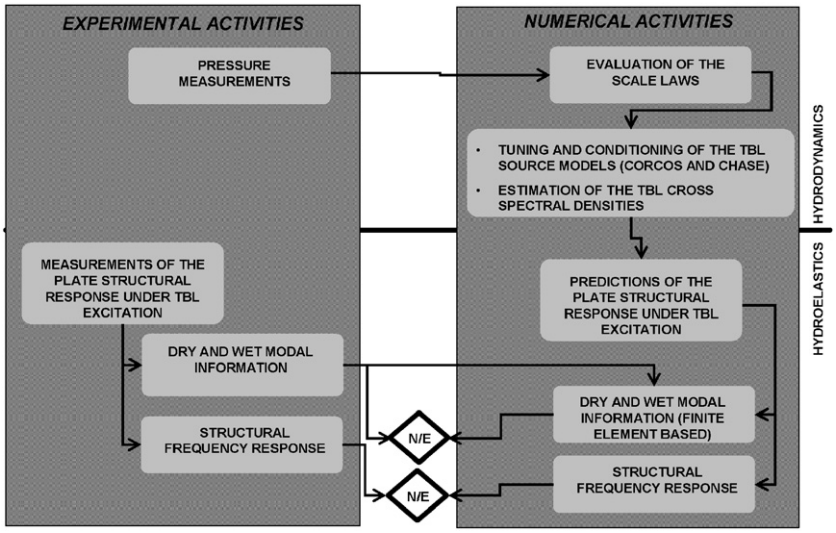

Chart 1. Logical workflow.

the length of the vessel along the waterline between the forward and aft perpendiculars, as depicted in Fig. 1. The maximum model width is 1.467 m, L_{pp} is 4.635 m and its draft in calm water conditions is 0.2 m.

The experiments were carried out in the INSEAN towing tank no. 2 which is 220 m long, 9 m wide and 3.5 m deep and is equipped with a carriage that can reach a maximum speed of 8 m/s. The use of this kind of facility creates ideal flow conditions because background turbulence and noise are avoided. The measuring section was chosen in the stern part of the ship bottom where the hull surface is almost flat. To perform pressure measurements a 2 cm thick rigid plexiglas plate was inserted in the hull bottom where pressure transducers were positioned.

The basic set-up is presented in Fig. 2 and consisted in an array of nine transducers in streamwise direction and five transducers in the spanwise direction flush-mounted with the plate at constant distance of 1 cm between each other. Additional tests were performed with 13 transducers mounted in streamwise direction within a maximum distance of 40 cm. Thus, the first pressure sensor was located at $x/L_{pp} = 0.88$ while the last at $x/L_{pp} = 0.97$. The minimum distance between transducers was constrained by the transducers' maximum external size while the maximum distance was chosen according to the fact that for $\xi/\delta^* > 20$ the longitudinal correlation is almost zero as demonstrated by previous measurements (Bull, 1967; Blake, 1986). Pressure signals were acquired in calm water conditions with fixed trim and sink and for two different ship model velocities: 3.31 m/s (25 knots) and 5.3 m/s (40 knots) corresponding to Fr = 0.49 and 0.78, respectively. The measurement error in the carriage velocity was within 1% of the nominal mean velocity.

Differential piezoresistive pressure transducers Endevco 8510-B, characterised by a maximum range of 2 psig and by a certified flat response until 14 kHz were used to measure pressure fluctuations. The transducers were statically calibrated in water using known water level heights. All the transducers showed a linear trend; however, the deviation around the regression line of the data points used for the sensitivity estimate was evaluated. The standard error of estimate was very low for all the transducers, of the order of 1%. Moreover, the total error due to thermal sensitivity, nonlinearity and pressure hysteresis, as reported in the data sheet, is around 1%. The rectangular sensing element has an area of $1 \times 0.3\,\text{mm}^2$, hence the effect of the finite size of the transducers surface can be expressed in term of the nondimensional parameters $d_0 = d/\delta^*$ and $d^+ = du_\tau/\nu$, where d is the bigger sensor dimension.

Pressure signals were acquired and amplified by the 16 channels acquisition system PROSIG; the sampling frequency was 12.5 kHz, the acquisition length was 15 s. Several repetitions of the test (typically 12–15) under nominally the same conditions were performed. The data record began a few seconds after the achievement of steady conditions. The

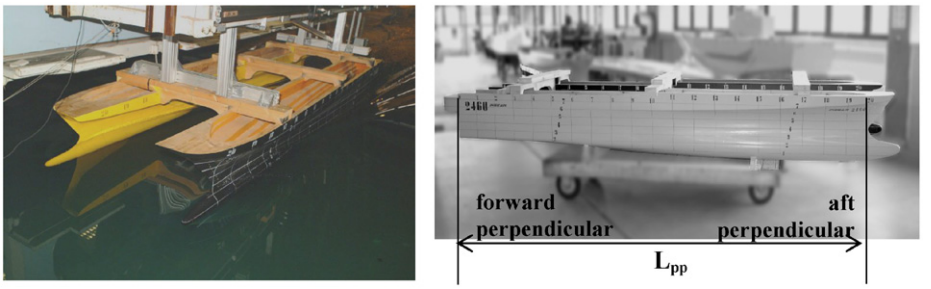

Fig. 1. Catamaran model and sketch of the reference length, L_{pp}.

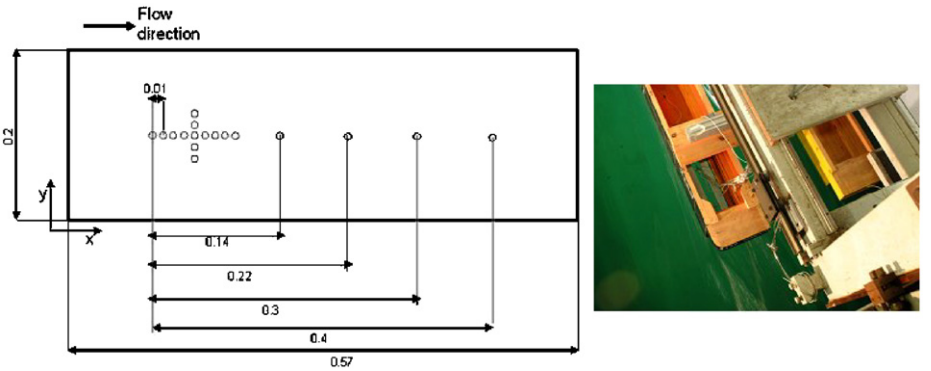

Fig. 2. Set-up for pressure measurements (left) and top view of the installation of the plexiglas plate (right).

Table 1
Mean flow velocity parameters: numerical estimation

U (knots)	U (m/s)	δ (m)	δ^* (m)	H	u_τ (m/s)	$\mathrm{Re}_\vartheta = U\vartheta/\nu$	$\mathrm{Re}_\tau = \delta u_\tau/\nu$	$d_0 = d/\delta^*$	$d^+ = du_\tau/\nu$
25	3.31	0.12	0.0142	1.27	0.11	29 535	10 153	0.07	84
40	5.31	0.113	0.0137	1.3	0.1626	42 807	14 133	0.073	125

reaching of a stationary random process was verified by comparing the ensemble average value, autocorrelation and cross-correlation of the WPFs of different runs.

Concerning the flow velocity field, the TBL mean parameters (as used in the data analysis and shown in Table 1) were obtained by available RANS simulations performed in the past over the whole model. This solution was, in this case, preferred because the experimental evaluation of the boundary layer velocity profiles in a towing tank, although possible, is a time-consuming process. In fact, it is clear that the acquisition time is limited for each carriage run, especially for the higher velocities, and that the time needed for the re-establishment of calm water conditions between two consecutive runs is at least 10 min. A detailed description of the numerical code is provided in Ciappi and Magionesi (2005) and in the references cited there. The numerical errors can be predictable in an uncertainty of about 4% in the estimation of the TBL parameters from the velocity profiles.

2.2. Vibration measurements

Vibration measurements were performed replacing the rigid plate with a flexible one. The panel, made of plexiglas, is 0.58 m long, 0.2 m wide and 0.003 m thick, it was fixed to the hull model with some mastic in order to provide impermeable conditions and to reduce the transmission of model vibrations.

A preliminary series of numerical analyses have been performed to exclude the presence of significant plate deformations due to static and dynamic pressure loads. In fact, for all the flow speeds under consideration, the maximum displacement was predicted to be 1% of the longitudinal plate dimension.

The acceleration responses were acquired in eight different points (one for each carriage run) randomly chosen on the plate surface. A Brüel & Kjaer piezoelectric accelerometer type 4393 characterised by a sensitivity of 4.19 mV/g and a weight of 2.2 g was used for the acquisition. Its mass was negligible with respect to the plate mass in the frequency range of interest. The accelerometer signal was amplified by a Brüel & Kjaer amplifier type 2635 and acquired with a sampling frequency of 12.5 kHz by a National Instruments PXI 6052E acquisition system. Preliminary dry and wet calm water tests were performed with the same set-up and instrumentation to evaluate the plate's natural frequencies, hence the added fluid mass and the modal damping factors. Two additional accelerometers were mounted on the ship's hull and on the connecting system to acquire the spurious vibrations transmitted by the carriage structure.

3. Pressure analysis

In the following sections, the results of the experimental programme devoted to the characterisation of wall-pressure spectra are presented. The purpose of this analysis was to verify the pressure scaling laws and to provide a general model for its spatial behaviour. To this aim, ASDs, streamwise and spanwise coherences and convection velocities were extracted from measurements. Although free surface effects were naturally present, pressure gradient values calculated on the basis of numerical simulations can be considered negligible in the measuring section. In Fig. 3, the velocity profiles obtained numerically, used to extract the mean TBL parameter values of Table 1, are shown in wall units y^+, u^+. From preliminary analysis it was decided to consider only the Corcos and Chase models as antagonists in this analysis. In fact, the Efimtsov model has the same trend as Corcos' in the low wavenumber domain but, this last is to be preferred because describes the wall pressure by a simpler expression containing less empirical parameters. The Ffowcs Williams model was built to extend Corcos model to the acoustic domain, which is beyond the purpose of this analysis; finally, the Smol'yakov and Tkachenko model does not fit well the present hydrodynamic data.

3.1. Power spectral density: scaling laws

The analysis of the scaling laws for the ASD is essential to understand the contribution of the different boundary layer regions to WPFs. Moreover, due to the particular section chosen to perform pressure measurements and the

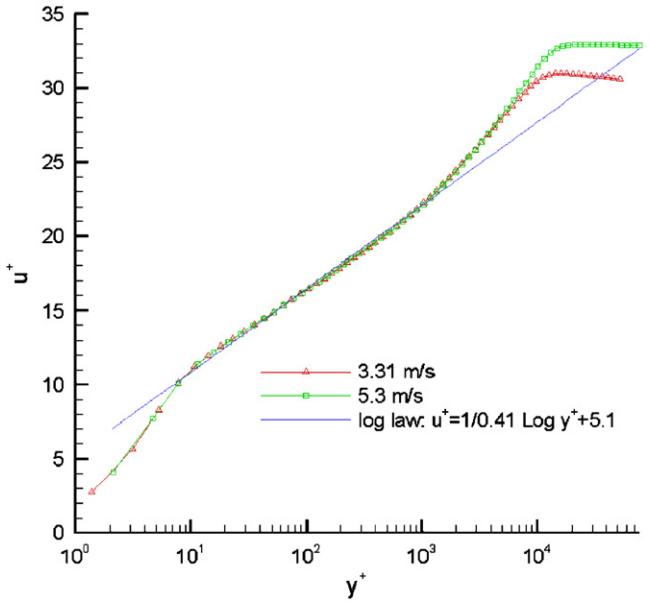

Fig. 3. Streamwise velocity profiles: numerical estimation.

relatively high speed of this vessel, local Reynolds numbers were sensibly high ($Re_\vartheta = 29\,535$ for 3.31 m/s and $Re_\vartheta = 42\,807$ for 5.31 m/s), providing an interesting extension of the validity of the scaling laws for high Reynolds number. Following the frequency range division proposed by Farabee and Casarella (1991), three different spectral regions can be identified: at very low frequency, the spectra collapse using the classical outer flow variables δ^* and U, showing a ω^2 behaviour, advising that sources are associated with the large-scale structures. In the low-mid-frequency range, the pressure auto spectral densities collapse into a single curve when scaled with the friction velocity u_τ, the wall shear stress τ_w and δ, implying that the mid-frequency structures are related with turbulence activity in the outer region of the boundary layer. In this interval, pressure spectra exhibit their maxima for $\omega\delta/u_\tau = 50$. Finally, at high-frequency inner variable scale, which employs u_τ, τ_w and ν, allows the collapse of the data independently of the Reynolds number, suggesting that sources are associated with the buffer region of the wall layer. Moreover, between mid- and high-frequency an overlap region, characterised by an ω^{-1} decay, exists where both outer and inner variable scales hold. This region is related to the turbulence activity in the logarithmic part of the boundary layer and its extension depends on the Reynolds number value. Recently, Ciappi and Magionesi (2005), considering the frequency division stated by Farabee and Casarella provided another confirmation of the proposed scaling laws. ASDs were determined using 700 spectral averages for each signal and a Hamming window function is used to reduce bandwidth leakage. According to classical theory of random data (Bendat and Piersol, 1991), the statistical convergence error was defined as $\varepsilon_r = 1/\sqrt{n_d}$, where n_d is the number of spectral averages. In the present analysis, the data random error was equal to $\pm 3.8\%$; thus, the uncertainty in the calculated pressure spectra, obtained by considering the above and all the previously defined experimental sources of error (see Section 2), was within the range of ± 1 dB.

In Fig. 4, a typical ASD signal is displayed showing high peaks in the frequency region between 8 and 20 Hz due to structural vibrations of the carriage and of the connecting system. The peaks were eliminated, for the ASD analysis, using suitable relations based on the coherence function (Bendat and Piersol, 1991) between two pressure sensors located sufficiently far from each other to be correlated only by structural vibrations. The result of this cleaning procedure is shown in the same figure. Fig. 5 shows the cleaned ASD for the two different test velocities, scaled using outer flow variables: $\omega\delta/u_\tau$, $\Phi_{pp}(\omega)u_\tau^2/\tau_w^2\delta$; they are shown and compared with the results of Farabee and Casarella (1991) obtained for $Re_\vartheta = 6050$ and with the results of Blake (1970) [extracted from Lee et al. (2005a)] obtained for $Re_\vartheta = 8210$. From the inspection of the figure, it is evident that there is an excellent agreement of the present experimental curves in the low-mid-frequency range, i.e. for $20 < \omega\delta/u_\tau < 1760$. Moreover, for $\omega\delta/u_\tau < 800$, they are in a very good agreement with the Farabee and Casarella curve and in fair agreement with the Blake data. Finally, the scaled spectra achieved the maximum value for $\omega\delta/u_\tau \approx 63$. Low-frequency behaviour ($\omega\delta/u_\tau < 5$) is not analysed, since frequency resolution is too poor to obtain a realistic trend in this region. Fig. 6 shows the present wall-pressure spectra and the results of Bull and Thomas (1976), Farabee and Casarella (1991) and Blake (1970) scaled on inner flow

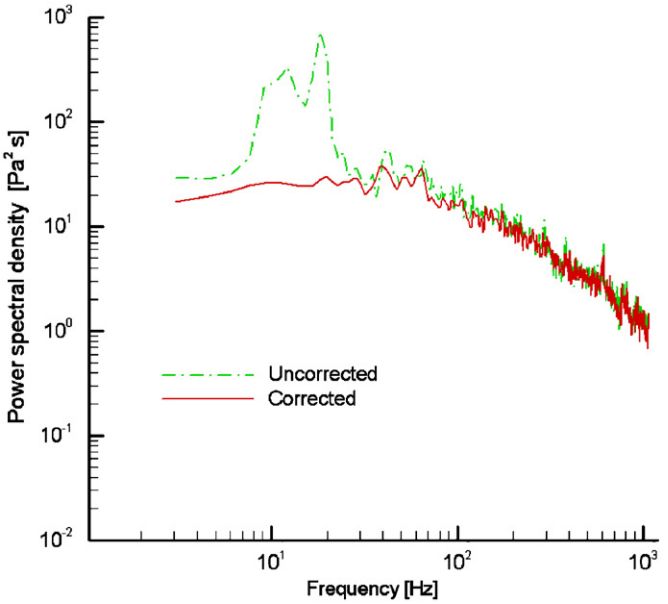

Fig. 4. Measured and cleaned pressure auto-spectral density.

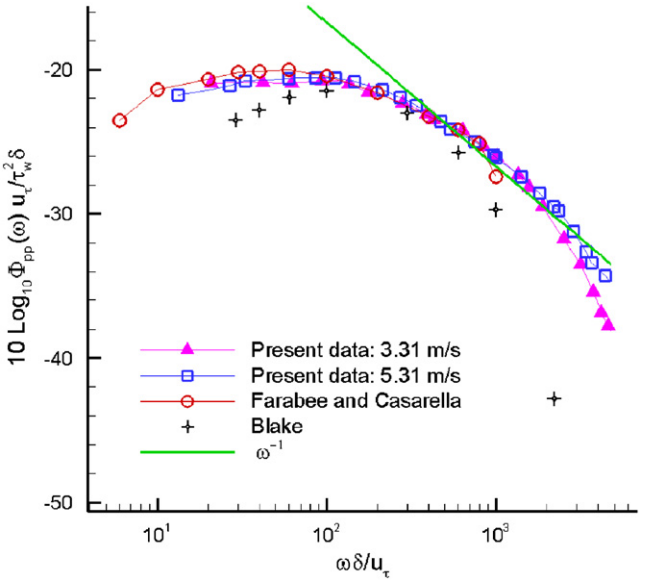

Fig. 5. Wall-pressure spectra scaled on outer flow variables.

variables: $\omega\nu/u_\tau^2$, $\Phi_{pp}(\omega)u_\tau^2/\tau_w^2\nu$. According to Blake (1986), attenuation in the spectra should occur approximately for $\omega d/U > 1.2$ that implies $\omega\nu/u_\tau^2 > 0.3$ or 0.42, depending on flow velocity. A collapse of the two sets of measurements occurs at high frequency, i.e. for $0.033 < \omega\nu/u_\tau^2 < 0.3$. The Bull and Thomas and Blake data are in excellent agreement in the same frequency range, although the Blake curve is higher for higher nondimensional frequencies. On the contrary, the Farabee and Casarella curve shows quite a different trend, characterised by slower high-frequency decay. Differences can be due to spectra attenuation caused by the finite sensor dimensions and, when considering similar d^+ values, to the use of different pressure transducers. In particular, the Farabee and Casarella and Blake data were obtained using open pinhole microphones with $d^+ = 33$ and 68, respectively, while the Bull and Thomas data were obtained using both filled pinhole microphones and piezoelectric transducers for $d^+ = 44$. For the present data,

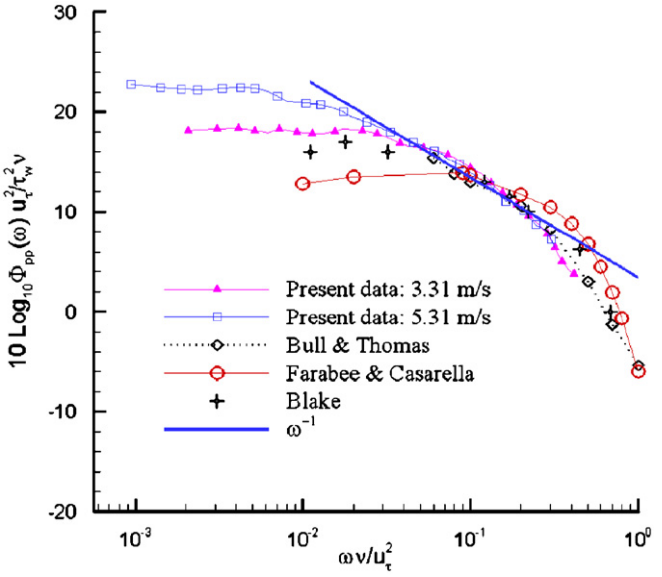

Fig. 6. Wall-pressure spectra scaled on inner flow variables.

obtained with piezoresistive pressure transducers, d^+ was equal to 84 for the lower velocity and to 125 for the higher. Bull and Thomas (1976) showed that the use of an open pinhole microphone leads to a higher amplitude of pressure spectra for $\omega\nu/u_\tau^2 > 0.1$. This fact can explain the mismatch between different sets of measurements. Finally, due to the high Reynolds numbers, the overlap region had a considerable extension. From the analysis of the range of validity of the outer and inner scales or from the direct inspection of the range of validity of the ω^{-1} law, included in both Figs. 5 and 6, it can be concluded that the overlap region extends in the range $0.033\,\mathrm{Re}_\tau = 335 < (\omega\delta/u_\tau) < 1760$ or $0.033 < (\omega\nu/u_\tau^2) < (1760/\mathrm{Re}_\tau) = 0.174$ where the lowest value of Re_τ was used.

3.2. Cross-spectral density

The spatial characterisation of WPFs is now analysed extracting from the experimental data the streamwise $\Phi_{pp'}(\xi, 0, \omega)$ and the spanwise $\Phi_{pp'}(0, \eta, \omega)$ CSDs. Since the CSD is a complex quantity, as usual, the coherence function $\Gamma(\xi, \eta, \omega) = |\Phi_{pp'}(\xi, \eta, \omega)| \Big/ \sqrt{\Phi_{pp}^{(1)}(\omega) \times \Phi_{pp}^{(2)}(\omega)}$, where in the square root appear the ASDs of the two pressure signals, is used to display the results and to discuss their comparison with the Corcos and Chase theoretical models. Coherence spectra were obtained for quite a large number of streamwise spacings ($0.09 \leqslant \xi/\delta \leqslant 1.44$), while only few spanwise separations were considered ($0.09 \leqslant \eta/\delta \leqslant 0.36$), as the coherence decay of the pressure field is very fast in this direction.

3.2.1. The Corcos model

The model formulated by Corcos expresses the CSD as a product of functions in longitudinal and lateral direction separately. Moreover, he postulated that the CSD behaviour depends only on the similarity variables $\omega\xi/U_c$ and $\omega\eta/U_c$ with a decay represented by an exponential function. The model for the CSD is given by

$$\Phi_{pp'}(\omega, \xi, \eta) = \Phi_{pp}(\omega)\, \mathrm{e}^{\mathrm{i}(\omega\xi/U_c)}\, \mathrm{e}^{-\gamma_1|\omega\xi/U_c|}\, \mathrm{e}^{-\gamma_3|\omega\eta/U_c|}, \tag{1}$$

where γ_1 and γ_3 are the decay factors.

The streamwise coherences relative to the free-stream velocity of 5.3 m/s are plotted against the CSD phase $\theta(\xi, \omega) = -\omega\xi/U_c$ in Fig. 7; different curves refer to different values of the nondimensional length ξ/δ. It is evident that at high frequency a collapse of the coherence spectra into an universal curve occurs independently of the spatial separation. The theoretical streamwise coherence $\Gamma(\xi, \omega) = \mathrm{e}^{(-\gamma_1|\omega\xi/U_c|)}$ derived from Eq. (1) is plotted in the same figure with a decay coefficient γ_1 equal to 0.125. Slightly different values are reported in the literature: Bull (1967) found $\gamma_1 = 0.1$, Farabee and Casarella (1991) found a decrease in the γ_1 value with increasing velocity passing from 0.145 for the lower one to 0.125 for the higher one. On the other hand, in the low-frequency region, a lack of similarity scaling

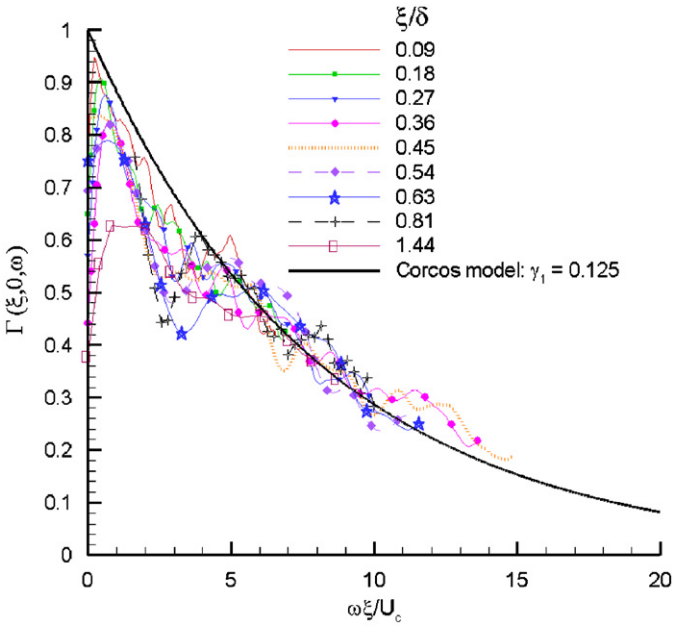

Fig. 7. Streamwise coherence at $U = 5.3$ m/s.

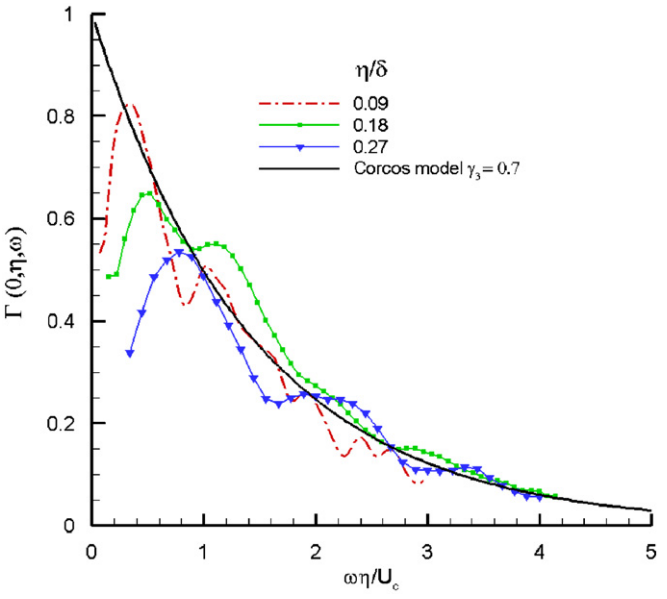

Fig. 8. Spanwise coherence at $U = 3.3$ m/s.

occurs because as far as $\omega\xi/U_c \to 0$ the coherences do not tend to unity as Corcos model predicts. Unit coherence would imply that the low-frequency components should be correlated for all spatial separations: this is physically unrealistic. From the observation of the figure it can also be noted that all curves exhibit a maximum that is indicated by Farabee and Casarella (1991) as the limit value below which the similarity variables do not hold anymore. The same considerations can be drawn for 3.3 m/s; in particular, the best fit of the experimental data is found for the same value of γ_1.

Less experimental data concerning spanwise coherence are available in the literature: the value usually suggested for the decay coefficient γ_3 is 0.7 (Corcos, 1963; Blake, 1986; Bull, 1967). Fig. 8 shows curves of spanwise coherence relative

to the lower velocity for various nondimensional separations η/δ as a function of the similarity variable $\omega\eta/U_c$. The thick solid line represents the Corcos model with γ_3 equal to 0.7. The exponential function seems to correctly estimate the measured coherences, above their maxima, for value of the nondimensional frequency $\omega\eta/U_c > 0.8$. Also in this case, velocity variations seem not to have an influence on the decay coefficient value.

3.2.2. The Chase model

A descriptive model of the wavenumber-frequency spectrum of turbulent wall-pressure was proposed by Chase (1980) with the intention of overcoming the limitations of models built to capture the characteristics of the convective domain only. Starting from the properties of the fluctuating velocity spectrum and considering its relation with the fluctuating pressure, Chase proposed a model able to correctly describe the pressure field in the convective and sub-convective domains. The inverse Fourier transform of the Chase (1980) expression is here proposed in its complete form as determined by Josserand and Lauchle (1989) because, as it will be clear in the following, the assumptions at the basis of some simplifications made by Chase are not necessarily fulfilled. Thus, the complete Chase model in the space-frequency domain is given by

$$
\begin{aligned}
&\Phi_{pp'}(\omega,\xi,\eta) = \Phi_{pp}(\omega)(C_m f_m \,\mathrm{e}^{-z_m}\,\mathrm{e}^{-\mathrm{i}(\omega\xi/U_m)} + C_t f_t \,\mathrm{e}^{-z_t}\,\mathrm{e}^{\mathrm{i}(\omega\xi/U_\tau)}),\\
&f_m = \frac{U_m}{\sqrt{U_c^2 + h_m^2 u_\tau^2}}\alpha_m^{-3}\left(1 + z_m + \alpha_m^2\mu_m^2\frac{1 - z_{m1}^2}{z_m} + 2\mathrm{i}\alpha_m\mu_m z_{m1}\right),\\
&f_t = \frac{U_t}{\sqrt{U_c^2 + h_t^2 u_\tau^2}}\alpha_t^{-3}\left(1 + z_t + \alpha_t^2\left(1 + \mu_t^2 - \frac{z_{t3}^2 + \mu_t^2 z_{t1}^2}{z_t}\right) + 2\mathrm{i}\alpha_t\mu_t z_{t1}\right),\\
&z_{m1} = \frac{\alpha_m\mu_m\omega\xi}{U_m},\quad z_{t1} = \frac{\alpha_t\mu_t\omega\xi}{U_t},\quad z_{m3} = \frac{\alpha_m\omega\eta}{U_m},\quad z_{t3} = \frac{\alpha_t\omega\eta}{U_t}, z_m = \sqrt{z_{m1}^2 + z_{m3}^2},\\
&z_t = \sqrt{z_{t1}^2 + z_{t3}^2},\\
&C_m = \frac{r_m}{r_t f_{t0} + r_m f_{m0}},\quad C_t = \frac{r_t}{r_t f_{t0} + r_m f_{m0}},\quad r_m = 1 - r_t,\\
&f_{m0} = \frac{U_m}{\sqrt{U_c^2 + h_m^2 u_\tau^2}}\alpha_m^{-3}(1 + \alpha_m^2\mu_m^2),\quad f_{t0} = \frac{U_t}{\sqrt{U_c^2 + h_t^2 u_\tau^2}}\alpha_t^{-3}(1 + \alpha_t^2(1 + \mu_t^2)),
\end{aligned}
\tag{2}
$$

$$
\begin{aligned}
&\Phi_{pp}(\omega) = r_m a_+ \rho^2 u_\tau^4 \omega^{-1}\alpha_m^{-3}\frac{U_m}{\sqrt{U_c^2 + h_m^2 u_\tau^2}}(1 + \mu_m^2\alpha_m^2) + r_t a_+ \rho^2 u_\tau^4\omega^{-1}\frac{U_t}{\sqrt{U_c^2 + h_t^2 u_\tau^2}}\alpha_t^{-3}(1 + \alpha_t^2(1 + \mu_t^2)),\\
&h_i = \frac{U_c\mu_i}{u_\tau\sqrt{1 - \mu_i^2}},\quad U_i = \frac{U_c}{1 - \mu_i^2},\quad \alpha_i^2 = \left[\frac{1}{1 - \mu_i^2}\right] + \left(\frac{U_i}{b_m\delta\omega}\right)^2,\quad i = m, t.
\end{aligned}
$$

It can be noted that six free parameters have to be determined by comparison with experimental data. The values suggested by Chase, based on the comparison between the experimental data of Bull (1967) and limiting values of Eq. (2), are the following: $b_m = 0.756$, $b_t = 0.378$, $\mu_m = 0.176$, $r_t = 0.389$, and $a_+ = 0.766$. As pointed out by Chase, these values are not supposed to be universal, as already shown for example by the measurements of Finnveden et al. (2005). In fact, the attempt to fit the experimental data with the Chase model using these values for the free parameters gave unsatisfactory results. Thus, the first five parameters were evaluated using a nonlinear least-square formulation based on a trust-region approach. The best fit of the experimental streamwise and spanwise coherences for both velocity conditions is found for: $b_m = 0.51$, $b_t = 0.35$, $\mu_m = 0.13$, $\mu_t = 0.4$, and $r_t = 0.3$. Fig. 9 presents the comparison among the experimental streamwise coherence for $U = 5.3$ m/s, the Chase model, using the identified parameters, and the Corcos model for different values of the ratio ξ/δ. In Fig. 10, the same comparison is shown for the spanwise coherence relative to $U = 3.3$ m/s. At this time, some considerations must be made: the coefficient b_m gives the position of the ASD maximum that, according to the present measurements occurs for $\omega\delta/u_\tau \approx 60$; on the other hand, using Chase relations, the maximum is given by $\omega = \sqrt{2}U_c/b_m\delta$, thus $b_m = 0.51$ is required if $U_c = 0.65U$ is assumed. In fact, the value 0.756 suggested by Chase represented an average between the value 0.53 needed to fit the maximum in the Bull spectrum, thus very close to that already found, and the value 0.9 needed to fit the measured spatial correlation. Preliminary comparisons between the experimental CSD and the simplified Chase model gave a value for the coefficient μ_t sensibly higher than that suggested by Chase. Thus, it was evident that the hypothesis $\mu_m, \mu_t \ll 1$ at the basis of the simplifications

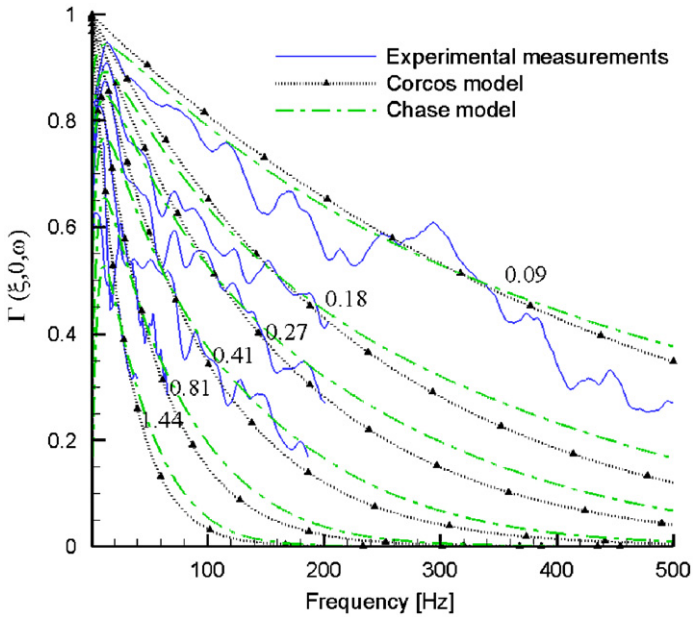

Fig. 9. Streamwise coherence: comparison with theoretical models.

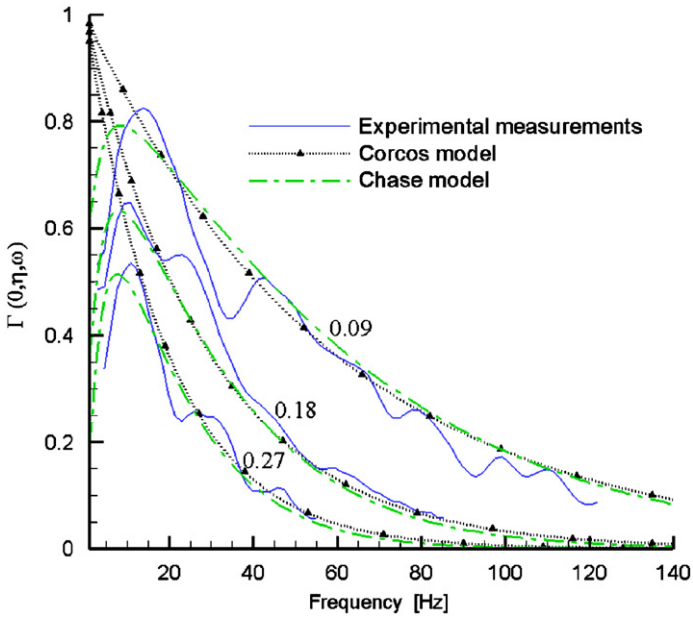

Fig. 10. Spanwise coherence: comparison with theoretical models.

made by Chase was, in this case, not valid. For this reason, the complete form as in Eq. (2) is used to perform the analysis. It can be concluded that, except for μ_t and somewhat for μ_m, the values of the identified parameters are not so far to those found by Chase analysing pressure experimental data acquired in completely different flow conditions.

Finally, a_+ is obtained by a direct comparison with the measured ASD (see Fig. 11) when the other coefficients are fixed. This parameter determines the amplitude of the ASD spectrum and in particular of its maximum, the best agreement with experimental data is found for $a_+ = 0.8$. On the other hand, if the interest is not in the maximum but in

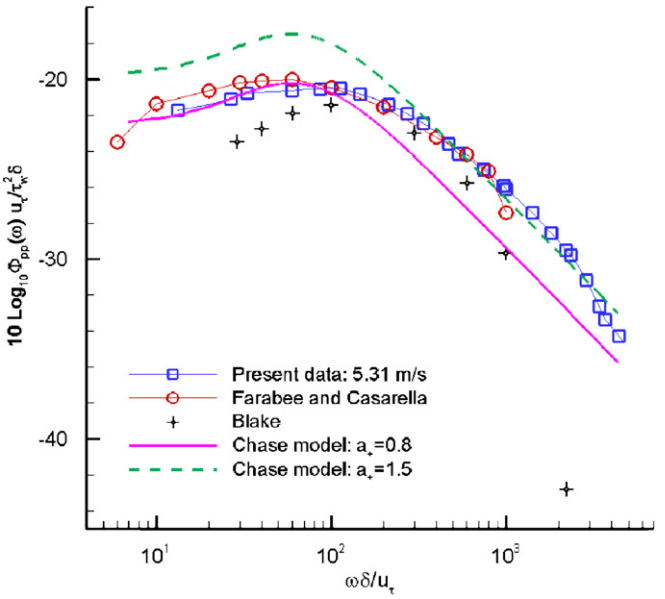

Fig. 11. Auto-spectral density: comparison with Chase model.

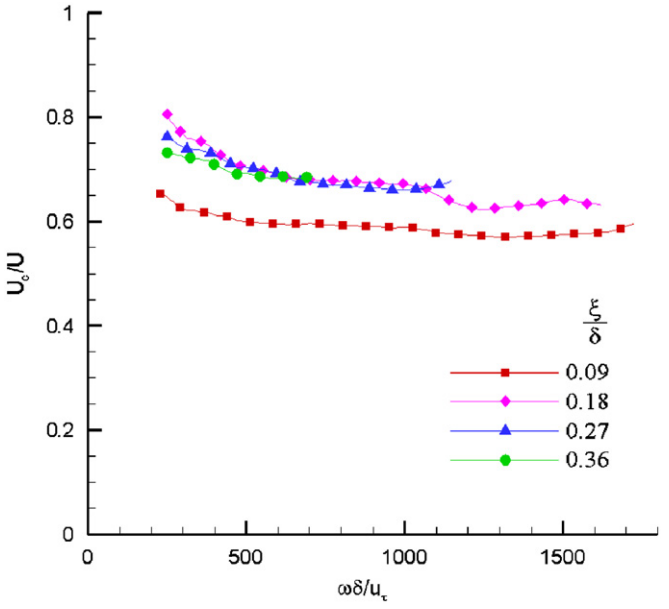

Fig. 12. Convection velocity at $U = 3.31$ m/s.

the higher frequency scale-independent region, the value of a_+ should be 1.5. However, to perform the structural analysis described in Section 4.3, the measured ASD was used.

3.3. Convection velocity

Some other insights into spectral characteristics of the WPFs can be provided by examining the convection velocity U_c. The convection velocity can be obtained from the phase $\theta(\xi, \omega) = -\omega\xi/U_c(\xi, \omega)$ of the CSD. In Figs. 12 and 13, the

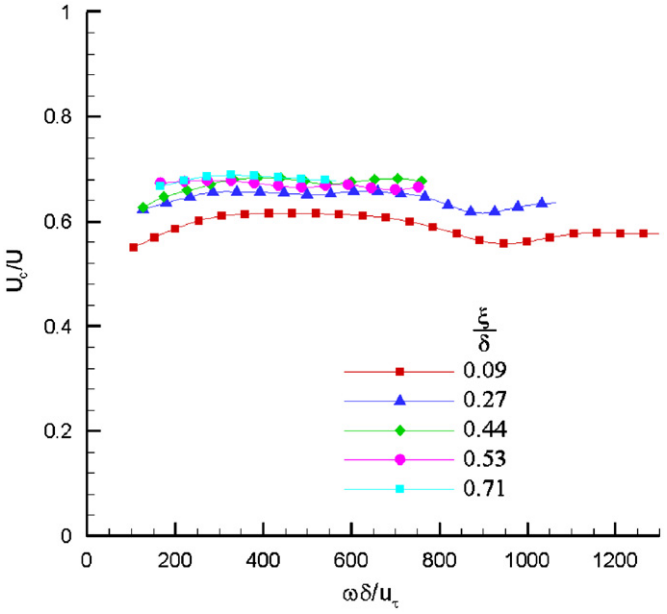

Fig. 13. Convection velocity at $U = 5.31$ m/s.

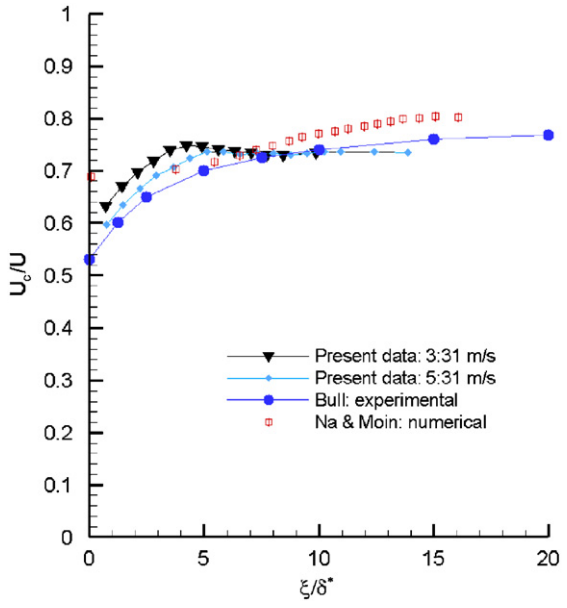

Fig. 14. Broadband convection velocity.

convection velocities divided by the free-stream velocity U, obtained for fixed spatial separations ξ/δ, are plotted as a function of the dimensionless frequency $\omega\delta/u_\tau$. Different figures refer, as usual, to the two different free-stream velocities. Farabee and Casarella (1991) have observed a peak value of convection velocity for $\omega\delta/u_\tau = 50$, independently of the ξ/δ values. This peak corresponds exactly to the maximum observed in the spectra and to the value that separates the low and the high-frequency behaviour in the coherence function. This fact demonstrated that not only the lowest wavenumber components experienced a decay, but that they are also convected at lower overall velocity. In the present case, CSD analysis was performed without using noise cancellation technique to avoid phase alteration.

On the other hand, convection velocity obtained by a division for the CSD phase is very sensitive to small disturbances leading to unreasonable value of the convection velocity. For this reason, frequencies below 25 Hz were cancelled out from the graph.

By inspection of Figs. 12 and 13, an increase of the convection velocity with the growing of the spatial separation is observed; this trend of U_c is related to an increasing dominance of large-scale events to the two-point correlation as the separation increases. For small separations, the correlation data and hence the convection velocity are dominated by the small-scale eddies close to the wall, which move with a lower velocity than the large-scale events. However, as far as spatial separation increases, the curves tend to collapse in a unique curve indicating that, even if the Taylor frozen flow hypothesis does not strictly hold for the smallest spatial separations, the convection velocity can be represented as a function of the single variable $\omega\delta/u_\tau$. Moreover, with increasing frequency, the convection velocities assume a flat trend.

The dependence of the convection velocity on the spatial separation can be better highlighted from the analysis of the space-time correlation functions of the pressure signals. The convection velocity is obtained as the ratio ξ/τ at which the cross-correlation $R_{pp}(\xi,\tau)$ has a maximum. In Fig. 14, the convection velocities normalised with respect to the free-stream velocity for 3.31 and 5.31 m/s are depicted as a function of the nondimensional parameter ξ/δ^*. The experimental data are also compared with those obtained experimentally by Bull (1967) and numerically by Na and Moin (1996). The values of U_c range from 0.6 for the smaller separations associated with the small-scale structures, to 0.73 at higher separations, related to the larger ones. From the above considerations, as proposed by several authors, the convection velocity can be modelled with a constant average value between small- and large-scale convection velocities, in this case, equal to 0.65 U.

4. Structural response analysis

4.1. Identification of modal parameters

Hammer impact tests were performed to determine dry and wet natural frequencies, and then the added fluid mass, modes and modal damping factors of the plate. The first 16 dry natural frequencies ω_{mn}, wet natural frequencies $\tilde{\omega}_{mn}$ and their correspondence with the mode shapes were evaluated in two specific frequency ranges: the dry set in 125–769 Hz and the wet one in the 26–283 Hz. Thus, the experimental function of the added mass, $m_f^e(\omega)$, was estimated by the relation (Blevins, 1987):

$$m_f^e(\omega) = \rho_s h\left[\left(\frac{\omega_{mn}}{\tilde{\omega}_{mn}}\right)^2 - 1\right]. \tag{3}$$

Since the pressure load spectra exhibited a significant energy content up to 1 kHz, the modal parameters were evaluated in a larger frequency range, 0–3 kHz, by using a FE model of the plate. The experimental boundary conditions were reproduced by imposing zero displacement and adding rotational springs along the plate edges; their stiffness was tuned in order to replicate the experimentally measured natural frequencies.

An approximated numerical/theoretical expression for the added mass, valid for structural waves having wavenumbers greater than the acoustic wavenumber $k = \omega/c$, is provided by the relation (Fahy, 1985)

$$m_f^n(\omega) = \frac{\rho}{k_s}, \tag{4}$$

where $k_s = \sqrt{k_m^2 + k_n^2}$ is the primary effective wavenumber component of the vibration. Hence, the numerical wet natural frequencies were computed by the following expression:

$$\tilde{\omega}_{mn} \cong \omega_{mn}\left(1 + \frac{\rho}{\rho_s h k_s}\right)^{-1/2}, \tag{5}$$

where ω_{mn} are the numerical dry natural frequencies computed by the aforementioned FE model. The primary wavenumber used in Eq. (5) corresponds to simply supported boundary conditions, i.e. $k_m = m\pi/a$ and $k_n = n\pi/b$ this last being the only one analytically known. It is clear that this assumption is valid as far as the frequency increases. In Fig. 15, the experimental and the theoretical added mass curves, $m_f^e(\omega)$ and $m_f^n(\omega)$, respectively, for the first 16 modes, are displayed showing a difference of about 23% for the first mode that decreases, as expected, with increasing mode order. Moreover, although natural modes of plates surrounded by unbounded fluids are not mathematically orthogonal, their shapes remain almost unchanged (Fahy, 1985). This result was partially verified by the experimental

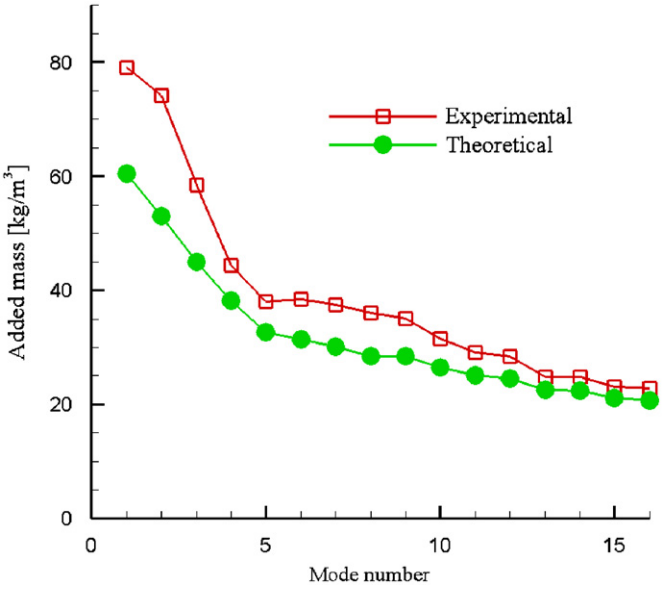

Fig. 15. Added mass coefficient.

analysis. In fact, a modal identification was performed using a number of points, sufficient to identify the mode order and the position of nodes and maxima along some selected lines, but not to represent the whole mode shapes.

In conclusion, to calculate the structural response with the numerical procedure described in the following section: (i) the dry modes provided by the FE analysis are used, (ii) the first 16 wet natural frequencies were obtained experimentally, and (iii) the remaining ones were estimated by using the dry natural frequencies provided by the FE analysis and Eq. (5).

The structural modal damping coefficient, η, was evaluated from wet hammer impact tests: it decreases from 0.034 for the first modes to a quite constant value around 0.018 for the higher modes.

4.2. Remarks on the prediction of structural response

A procedure based on the finite element approach was presented and discussed in the recent literature to solve the response of a plate under a TBL excitation (De Rosa and Franco, 2007). Specifically, the Corcos model was used for comparing the numerical response with the exact one, and in order to define a general methodology, able to work for any TBL model at acceptable computational costs. For the sake of clarity, some details are herein briefly recalled.

The cited finite element procedure is assembled by using the following equation suitable for all the methods working with discrete coordinates (Elishakoff, 1983); the CSD matrix of displacements of a structural operator represented by using NG degrees of freedom and NM mode shapes is given by

$$\mathbf{S_W}(\omega) = \mathbf{\Phi H}(\omega)\mathbf{S_\Phi}(\omega)\mathbf{H}(\omega)^* \mathbf{\Phi}^{\mathrm{T}}, \tag{6}$$

with

$$\mathbf{S_\Phi}(\omega) = \mathbf{\Phi}^{\mathrm{T}}\,\mathbf{S_{FF}}(\omega)\mathbf{\Phi}, \tag{7}$$

where $\mathbf{\Phi}$ is the structural modal matrix (each column is an eigenvector sampled at the NG selected points), $[NG \times NM]$ and the generic term of $\mathbf{H}(\omega)$ is $H_j(\omega) = [\omega_j^2 - \omega + \mathrm{i}\eta\omega_j^2]^{-1}$, $[NM \times NM]$.

The translation of the distributed random loads to the set of NG points, in other words the way of representing the $\mathbf{S}_{\mathrm{FF}}$, can be solved in the framework of the finite element method by using consistent approach, that is by using the shape function vector, $\mathbf{N}$, belonging to each element:

$$\mathrm{SC}^{(E)}_{FF\,k,q} = \int_{x_1^{(k)}}\int_{x_2^{(k)}}\int_{x_1^{(q)}}\int_{x_2^{(q)}} \mathbf{N}^{\mathrm{T}} \Phi_{pp'}(x_1^{(k)}, x_2^{(k)}, x_1^{(q)}, x_2^{(q)}, \omega)\mathbf{N}\mathrm{d}x_1^{(k)}\,\mathrm{d}x_1^{(q)}\,\mathrm{d}x_2^{(k)}\,\mathrm{d}x_2^{(q)}, \tag{8}$$

where the double integers k and q indicate here two generic finite elements and the integration is related to the area of each of them. The vector $\mathbf{N}$ can be interpreted as the interpolating function basis selected by the analyst according to the specific problem and boundary conditions (Cook, 1981). Thus, Eq. (8) serves to evaluate a generic kqth member of the $NE \times NE$ load matrix, where NE is the number of elements. A simplified approach could refer to each grid point rather than each finite element. This means that the load acting on the ith grid point will be the resultant of the distributed load working on the equivalent nodal area, say Area_i, belonging to it. This area vector can be evaluated easily by using a static deterministic unit pressure load (De Rosa et al., 1994; Hambric et al., 2004). Accordingly, one gets the generic ijth member of the $\text{NG} \times \text{NG}$ matrix:

$$\text{SC}^{(G)}_{FF\,i,j} = \int_{x_i-(\Delta x/2)}^{x_i+(\Delta x/2)} \int_{x_j-(\Delta x/2)}^{x_j+(\Delta x/2)} \int_{y_i-(\Delta y/2)}^{y_i+(\Delta y/2)} \int_{y_j-(\Delta y/2)}^{y_j+(\Delta y/2)} \Phi_{pp'}(x_i, x_j, y_i, y_j, \omega)\mathrm{d}y_j\,\mathrm{d}y_i\,\mathrm{d}x_j\,\mathrm{d}x_i. \tag{9}$$

An area $\Delta x \Delta y$ is assigned to both points $P(x_i, y_i)$ and $Q(x_j, y_j)$ and the double space integration refers to these finite domains. A further approximation could also be introduced, considering that the wall-pressure distribution due to the TBL in the low-frequency range does not fluctuate very quickly. In this case, the last integral could be approximated as follows:

$$\text{SL}^{(G)}_{FF\,i,j} = \Phi_{pp'}(x_i, x_j, y_i, y_j, \omega)[\Delta x \Delta y]^2. \tag{10}$$

Obviously, the approximations represented by Eqs. (8)–(10) are associated with decreasing computational cost.

The problem of the plate response under a convective random load, expressed in discrete form as described by Eqs. (6) and (7), can be accurately approached only when adequately resolving both the spatial distributions of the response function and of the forcing function; in particular, since in this case $U_c \ll c_B$, the discretisation length, is ruled by the hydrodynamic load.

In this work, Eq. (9) was used to calculate the $\mathbf{S}_{\text{FF}}$ matrix because Eq. (10) was not adequate for the present simulations. In fact, in the frequency range of interest, Eq. (9) allows the avoidance of the numerical divergence of the structural response due to the incorrect representation of the pressure load, as approximated by Eq. (10). Some further details of the numerical simulations are given in the next paragraph. The finite element approach was used to generate the modal base, while the responses were calculated by a specific Fortran code.

4.3. Experimental analysis and comparisons

The ASDs of the acceleration signals, experimentally measured in eight different points over the plate, were computed and the results averaged and compared with the results obtained by the numerical procedure exposed in the previous section. The numerical results were obtained applying Eqs. (6), (7) and (9) for both the Corcos and Chase models.

The FE analysis was performed using 61×21 grid points corresponding to a spatial discretisation of 1 cm in both directions. The integral in Eq. (9) was calculated using the trapezoidal rule. The hydrodynamic parameters inserted in Eq. (9) were those identified in Sections 3.1–3.3; in particular, the experimental ASD was used and the convection velocity was assumed constant over the whole frequency range and equal to $0.65U$ for both ship speeds. After having performed the convergence analysis, each integration domain was finally subdivided, for both velocity conditions, in eight intervals when the Corcos model was used and in 24 intervals when the Chase model was used instead. The Corcos numerical solution of integral in Eq. (9) was compared and validated by an analogous analytical solution (De Rosa and Franco, 2007). In both cases, the number of retained natural modes was 100.

The response of the plate was computed for a frequency range between 1 and 1000 Hz (the step was 4.5 Hz) for the higher velocity and only between 1 and 600 Hz for the lower one, because above this frequency a refined mesh must be used to obtain convergence. In these frequency ranges, the ratio between the bending wavenumber $k_B = \sqrt[4]{\rho_s h/D}\sqrt{\omega}$ and the convective wavenumber k_c (see Fig. 16) varied between 0.045 and 0.21 for the lowest velocity and between 0.057 and 0.35 for the highest velocity.

Figs. 17 and 18 present the experimental and numerical averaged ASDs of the plate's acceleration for 3.3 and 5.3 m/s, respectively.

Unsurprisingly, an overestimation of the plate response is evident in the whole frequency range if the Corcos model is used; on the other hand, the numerical response obtained using the Chase model is undoubtedly in better agreement with experimental data. However, below 25–30 Hz both pressure spectra (although cleaned) and structural response are contaminated by the carriage vibrations transmitted to the model; thus, any comparison is meaningless. Above these frequencies, the agreement is really satisfactory until 420 Hz for the lower velocity case and until 650 Hz for the higher one. In the high-frequency part, the Chase model tends to slightly underestimate the experimental curve; this fact, more

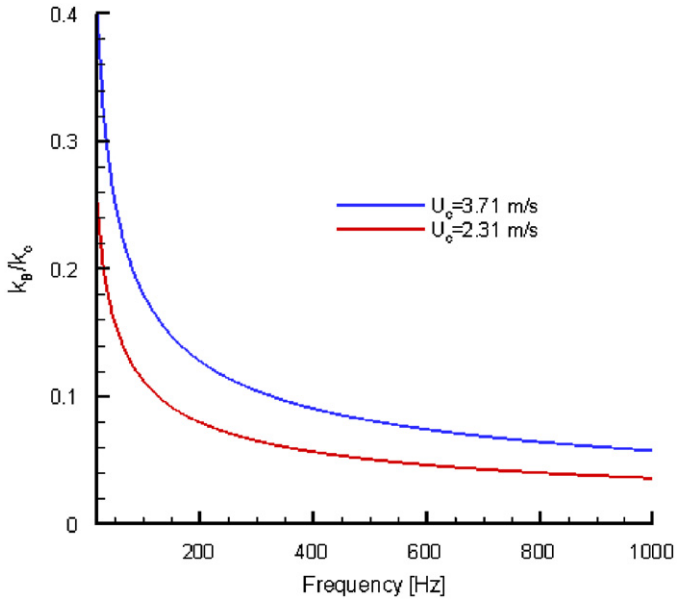

Fig. 16. Bending and convective wavenumber ratio.

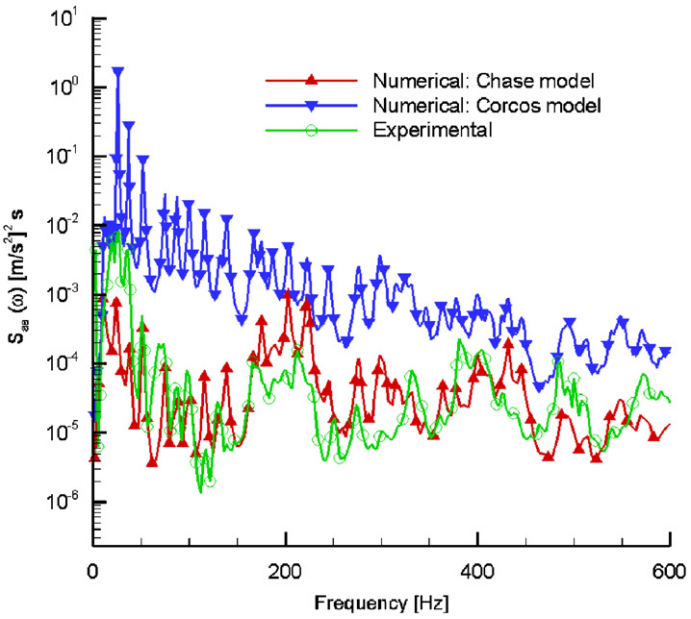

Fig. 17. Acceleration response spectra at $U = 3.3$ m/s.

visible for 3.3 m/s, can be partly due to the poor spatial resolution of pressure transducers that attenuate the high-frequency part of the ASD spectrum.

Finally, an evident mismatch between the experimental and the numerical curve, generated by the presence of high peaks in the experimental data, can be observed in Fig. 18 around 800 Hz probably due to local flow disturbances. To better quantify the difference between model and experimental results, the previous curves are plotted in Figs. 19 and 20 in third-octave bands. It can be seen that the root mean square of the difference between the response obtained applying the Chase model and the experimental data is 5.2 dB for the lower velocity and 4.1 for the higher one. The response obtained by using the Corcos model to represent the surface pressure field, overpredicts in both cases the experimental

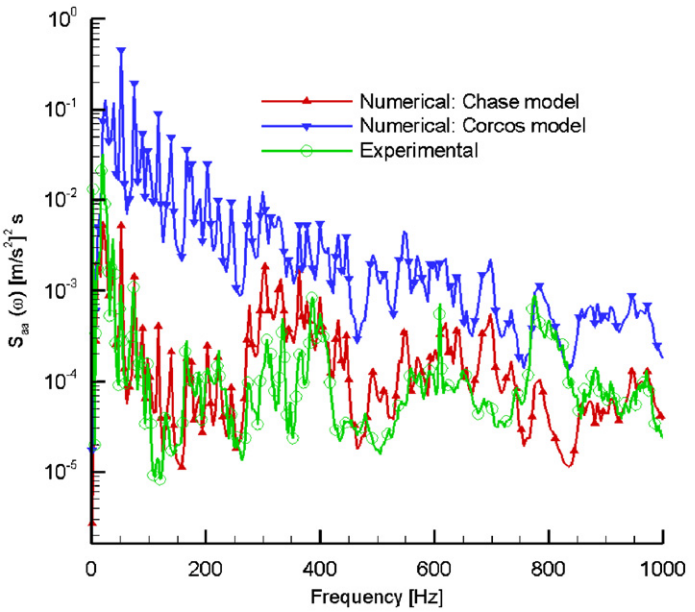

Fig. 18. Acceleration response spectra at $U = 5.3$ m/s.

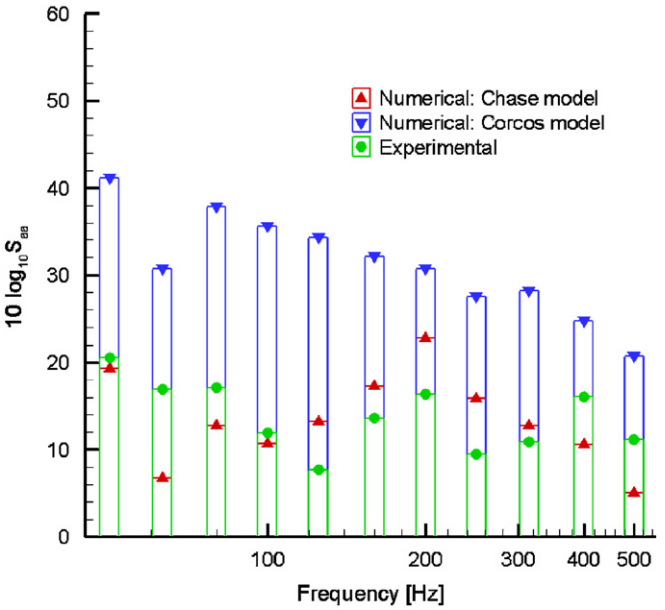

Fig. 19. Acceleration response spectra at $U = 3.3$ m/s, third-octave bands.

data resulting in an average difference of 18 dB. The small gap between the numerical predictions obtained by applying the Chase model and the experimental plate response that is less or, at least, of the same order of that found by Finnveden et al. (2005) demonstrated the validity of the developed procedure and the capability of the Chase model to represent the surface pressure field on a ship hull. However, a more careful determination of the added water mass in the whole frequency range can improve the numerical estimation, as well as a deep uncertainty analysis can better indicate the confidence interval of the present results.

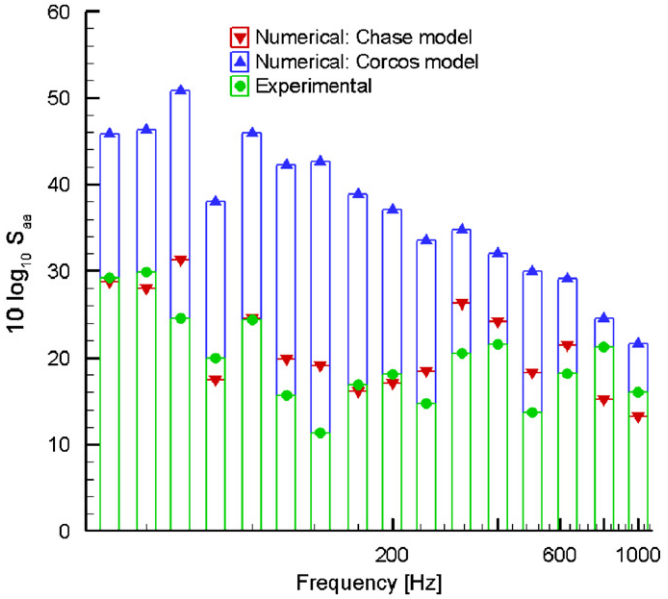

Fig. 20. Acceleration response spectra at $U = 5.3$ m/s, third-octave bands.

5. Concluding remarks

In this paper, a complete analysis of the coupled structural-fluid problem concerning the response of an elastic plate inserted in the bottom of a catamaran hull excited by the TBL WPFs, has been carried out.

The hydrodynamic analysis, performed on a rigid plate at high Reynolds number and in equilibrium flow conditions allowed the determination of the appropriate scaling laws for the ASDs in the different frequency ranges. Moreover, the analysis of the cross-spectral densities in longitudinal and lateral flow directions was used to fit the theoretical models, available for the pressure representation, to the experimental data. Two theoretical models are analysed: the Corcos and Chase models. It was demonstrated that it is possible to find for both a complete set of free parameters that provide a fair agreement with experimental CSD data.

Since spatial resolution was too poor to analyse the CSD behaviour at high frequency and since with this type of experimental analysis it was not possible to isolate the longest wavelengths, the studied pressure behaviour mainly concerned the characteristics of the convective domain. Thus, an indirect comparison based on the vibrational response of a plate was performed; in particular, the numerical structural responses obtained using the two models were compared with experimental measurements. The conclusion of this analysis is that, although the Chase model is complex and dependent on several empirical parameters, it provides a very good agreement with experimental data at low wavenumbers. The performed analysis can give interesting information also for the full-scale problem; in fact, considering realistic values of the hydrodynamic and of the structural parameters, coincidence conditions usually appear at very low frequency both for underwater and surface marine vehicles.

The main disadvantage in using Chase model lies in its non-predictive character. In fact, it was shown that the original Chase parameters do not fit the experimental data; thus a new set of parameters have been determined and the complete version of the model has been used.

It is clear that the aim of any numerical procedure is to produce robust predictive tools to be used at the design stage. Ongoing comparisons between pressure measurements performed on different ship models and for various flow conditions in terms of Reynolds number values are aimed to analyse the range of variability of the parameters and their dependence on the particular flow conditions.

Acknowledgement

The research was supported by the Ministero dei Trasporti in the frame of ‘‘Programma Ricerche Luglio2006-Dicembre 2007’’.

References

Abraham, B.M., 1998. Direct measurements of the turbulent boundary layer wall pressure wavenumber-frequency spectra. ASME Journal of Fluids Engineering 120, 29–39.

Bendat, J.S., Piersol, A.G., 1991. Random Data: Analysis and Measurements Procedure. Wiley, New York.

Blake, W.K., 1970. Turbulent boundary-layer wall-pressure fluctuations on smooth and rough walls. Journal of Fluid Mechanics 44, 637–660.

Blake, W.K., 1986. Mechanics of Flow Induced Sound and Vibration. Academic Press, Orlando.

Blevins, R.D., 1987. Formulas for Natural Frequency and Mode Shape. Robert E. Krieger Publishing Company, Melbourne, FL.

Bull, K.M., 1967. Wall pressure fluctuations associated with subsonic turbulent boundary layer flow. Journal of Fluid Mechanics 28, 719–754.

Bull, M.K., 1996. Wall pressure fluctuations beneath turbulent boundary layers: some reflections on forty years of research. Journal of Sound and Vibration 190, 299–315.

Bull, M.K., Thomas, S.W., 1976. High frequency wall pressure fluctuations in turbulent boundary layers. Physics of Fluids 19, 597–599.

Chang, P.A., Piomelli, U., Blake, W.K., 1999. Relationship between wall pressure and velocity-field sources. Physics of Fluids A 11, 3434–3448.

Chase, D.M., 1980. Modelling the wavevector-frequency spectrum of turbulent boundary layer wall pressure. Journal of Sound and Vibration 70 (1), 29–67.

Choi, H., Moin, P., 1990. On the space-time characteristics of wall pressure fluctuations. Physics of Fluids A 2, 1450–1460.

Ciappi, E., Magionesi, F., 2005. Characteristics of the turbulent boundary layer pressure spectra for high speed vessels. Journal of Fluids and Structures 21, 321–333.

Cook, R.D., 1981. Concept and Application of Finite Element Analysis. Wiley, New York.

Corcos, G.M., 1963. Resolution of pressure in turbulence. Journal of the Acoustical Society of America 35, 192–199.

De Rosa, S., Franco, F., 2007. Exact and numerical responses of a plate under a turbulent boundary layer excitation. Journal of Fluids and Structures 24, 212–230.

De Rosa, S., Pezzullo, G., Lecce, L., Marulo, F., 1994. Structural acoustic calculations in the low frequency range. AIAA Journal of Aircraft 31 (6), 1387–1394.

Efimtsov, B.M., 1982. Characteristics of the field of turbulent wall pressure fluctuations at large Reynolds numbers. Soviet Physics-Acoustics 28 (4), 289–292.

Elishakoff, I., 1983. Probabilistic Methods in the Theory of Structures. Wiley, New York.

Fahy, F., 1985. Sound and Structural Vibration. Academic Press, Orlando.

Farabee, T.M., Casarella, M.J., 1991. Spectral features of wall pressure fluctuations beneath turbulent boundary layers. Physics of Fluids A 3, 2410–2420.

Farabee, T.M., Geib, F.E., 1991. Measurements of boundary layer pressure fluctuations at low wavenumbers on smooth and rough walls. In: ASME Symposium on Flow Noise Modelling, Measurements and Control, NCA-vol. 11, FED-vol. 130, pp. 55–68.

Ffowcs Williams, J.E., 1982. Boundary layer pressures and the Corcos model: a development to incorporate low wavenumber constraints. Journal of Fluid Mechanics 125, 9–25.

Finnveden, S., Birgersson, F., Ross, U., Kremer, T., 2005. A model of wall pressure correlation for prediction of turbulence-induced vibration. Journal of Fluids and Structures 20, 1127–1143.

Goody, M., 1999. An experimental investigation of pressure fluctuations in three-dimensional turbulent boundary layers. Ph.D. Thesis, Department of Aerospace and Ocean Engineering, Virginia Tech, USA.

Graham, W.R., 1997. A comparison of models for the wavenumber-frequency spectrum of turbulent boundary layer pressures. Journal of Sound and Vibration 206 (4), 541–565.

Hambric, S.A., Hwang, Y.F., Bonness, W.K., 2004. Vibrations of plates with clamped and free edges excited by low-speed turbulent boundary layer flow. Journal of Fluids and Structures 19, 93–110.

Han, F., Bernhard, R.J., Mongeau, L.G., 1999. Prediction of flow-induced structural vibration and sound radiation using energy flow analysis. Journal of Sound and Vibration 227 (4), 685–709.

Hwang, Y.F., Maidanik, G., 1990. A wavenumber analysis of the coupling of a structural mode and flow turbulence. Journal of Sound and Vibration 142, 135–152.

Keith, W.L., Hurdis, D.A., Abraham, B.M., 1992. A comparison of turbulent boundary layer wall-pressure spectra. ASME Journal of Fluids Engineering 114, 338–347.

Josserand, M.A., Lauchle, G.C., 1989. ERRATA: D.M. Chase JSV 1980. Journal of Sound and Vibration 128, 519–523.

Lee, Y.T., Blake, W.K., Farabee, T.M., 2005a. Modeling of wall pressure fluctuations based on time mean flow field. ASME Journal of Fluids Engineering 127, 233–240.

Lee, Y.T., Miller, R., Gorski, J., Farabee, T., 2005b. Predictions of hull pressure fluctuations for a ship model. In: Proceedings of International Conference on Marine Research and Transportation (ICMRT05), Ischia, Italy.

Manoha, E., 1996. The wavenumber-frequency spectrum of the wall pressure fluctuations beneath a turbulent boundary layer. In: Proceedings of the AIAA Aeroacoustics Conference, AIAA paper 96-1758.

Na, Y., Moin, P., 1996. Direct numerical simulation of turbulent boundary layers with adverse pressure gradients and separation. Report No. TF-68. Thermosciences Division, Department of Mechanical Engineering, Stanford University.

Panton, R.L., Robert, G., 1994. The wavenumber-phase velocity representation for the turbulent wall-pressure spectrum. ASME Journal of Fluids Engineering 116, 477–483.

Smol'yakov, A.V., Tkachenko, V.M., 1991. Model of pseudosonic turbulent wall pressures and experimental data. Soviet Physics-Acoustics 37 (6), 627–631.

Willmarth, W.W., Wooldridge, C.E., 1962. Measurements of the fluctuating pressure at the wall beneath a thick turbulent boundary layer. Journal of Fluid Mechanics 14, 187–210.